

1 **Directly Measured Heating Rates of a Tropical Subvisible Cirrus Cloud**

2

3 **Anthony Bucholtz<sup>1\*</sup>, Dennis L. Hlavka<sup>2</sup>, Matthew J. McGill<sup>3</sup>, K. Sebastian Schmidt<sup>4</sup>,**

4 **Peter Pilewskie<sup>4</sup>, Sean M. Davis<sup>5</sup>, Elizabeth A. Reid<sup>1</sup>, and Annette L. Walker<sup>1</sup>**

5

6 <sup>1</sup>Naval Research Laboratory, Monterey, CA

7 <sup>2</sup>Science Systems and Applications, NASA Goddard Space Flight Center, Greenbelt, MD

8 <sup>3</sup>NASA Goddard Space Flight Center, Greenbelt, MD

9 <sup>4</sup>University of Colorado, Boulder, CO

10 <sup>5</sup>NOAA Earth System Research Laboratory, Boulder, CO

11

12

13

14

15

16

17

18

19

---

20 \*Corresponding Author: Anthony Bucholtz, Marine Meteorology Division, Naval  
21 Research Laboratory, 7 Grace Hopper Ave., Stop 2, Monterey, CA 93943-5502 Tel: 831-  
22 656-5024, Fax: 831-656-4769, Email: [anthony.bucholtz@nrlmry.navy.mil](mailto:anthony.bucholtz@nrlmry.navy.mil)

23

23 **Abstract**

24 We present the first direct measurements of the infrared and solar heating rates of a  
25 tropical subvisible cirrus (SVC) cloud sampled off the east coast of Nicaragua on 25 July  
26 2007 by the NASA ER-2 aircraft during the Tropical Composition, Cloud and Climate  
27 Coupling Experiment (TC4). On this day a persistent thin cirrus layer, with mostly clear  
28 skies underneath, was detected in real-time by the cloud lidar on the ER-2 and the aircraft  
29 was directed to profile down through the SVC. Measurements of the net broadband  
30 infrared irradiance and spectrally integrated solar irradiance above, below, and through  
31 the SVC are used to determine the infrared and solar heating rates of the cloud. The lidar  
32 measurements show that the variable SVC layer was located between ~13-15 km. Its  
33 midvisible optical depth varied from 0.01-0.1 with a mean of 0.0342 and a standard  
34 deviation of 0.0328. Its depolarization ratio was approximately 0.4, indicative of ice  
35 clouds. From the divergence of the measured net irradiances the infrared heating rate of  
36 the SVC was determined to be  $\sim 2.50\text{-}3.24 \text{ K day}^{-1}$  and the solar heating rate was found to  
37 be negligible. These values are consistent with previous indirect observations of other  
38 SVC and with model-generated heating rates of SVC with similar optical depths. This  
39 study illustrates the utility and potential of the profiling sampling-strategy employed  
40 here. A more fully instrumented high altitude aircraft that also included in situ cloud and  
41 aerosol probes would provide a comprehensive dataset for characterizing both the  
42 radiative and microphysical properties of these ubiquitous tropical clouds.

43

44

## 44 **1. Introduction**

45 Subvisible cirrus (SVC) are high altitude, optically thin ice clouds that are very  
46 common in the tropics. They are called subvisible because they are difficult to see  
47 visually from below or above and only become apparent when viewed edge-on, as when  
48 looking towards the horizon from an airplane. As a general rule of thumb it has been  
49 estimated that a visible cloud optical depth of approximately 0.03 is the minimum  
50 threshold for visual observation of these clouds (Sassen and Cho, 1992).

51 The extent and prevalence of subvisible cirrus was first detected by ground based  
52 lidar measurements in the western tropical Pacific at Kwajalein Atoll in the 1970s (Uthe  
53 and Russel, 1976). Subsequent satellite (Prabhakara et al., 1993; Wang et al., 1996;  
54 Winker and Trepte, 1998; Dessler et al., 2006; Mace et al., 2009), aircraft lidar  
55 (McFarquhar et al., 2000; Pfister et al., 2001) and ground-based lidar (Comstock et al.,  
56 2002) studies have confirmed the prevalence of SVC in the tropics and found that they  
57 are present approximately 30-50% of the time depending on location. These studies have  
58 also found that the SVC are located near the tropopause at altitudes of 14-17 km and are  
59 typically less than a kilometer thick. They can be variable in space and time or they can  
60 extend for hundreds of kilometers across the sky and last for several days. SVC have  
61 been detected as a single isolated layer or as a layer above deep convection. Ground-  
62 based lidar studies have also detected subvisible cirrus at mid-latitudes (Sassen et al.,  
63 1989; Sassen and Cho, 1992; Sassen and Campbell, 2001; Immler and Schrems, 2002)

64 Since their discovery over thirty years ago there have only been a few direct aircraft  
65 measurements of SVC, and these have been limited to measurements of the  
66 microphysical properties of the clouds. Heymsfield (1986) performed the first in situ



67 measurements of SVC acquiring data on the habits and sizes of the ice crystals in the  
68 cloud from a WB-57 aircraft over Kwajalein in 1973. Since then only a few in situ  
69 aircraft microphysical measurement studies have been performed (Booker and Stickel,  
70 1982; Peter et al., 2003; Lawson et al., 2007). More recently, Davis et al. (2010, this  
71 issue) report on aircraft in situ and lidar measurements of the microphysical properties of  
72 a subvisible cirrus made from the NASA WB-57 aircraft during the TC4 field study near  
73 Costa Rica focusing on the 6 August 2009 flight, a different SVC case than discussed in  
74 this paper.

75 This lack of measurements has left many uncertainties about the radiative and  
76 microphysical properties and effects of subvisible cirrus, and about their formation and  
77 persistence mechanisms. However, because of the prevalence of SVC in the tropics,  
78 several studies have suggested that these clouds may play an important role in the  
79 radiative balance of the tropical upper troposphere and in stratosphere-troposphere  
80 exchange by absorbing outgoing thermal infrared (IR) radiation and causing a subsequent  
81 modification of the thermodynamic structure of the upper troposphere (Gage et al., 1991;  
82 Jensen et al., 1996b; Rosenfield et al., 1998; Corti et al., 2006). This heating of the cloud  
83 layer may also play a role in the persistence of the SVC by either warming the cloud and  
84 causing it to dissipate in a matter of hours or by inducing a lifting of the cloud and  
85 causing it to persist for days (Jensen et al. 1996a). Two recent modeling studies have  
86 suggested that the IR heating of the SVC thermally forces a mesoscale circulation that  
87 enables the cloud to maintain itself for up to 2 days (Durrán et al., 2009; Dinh et al.,  
88 2009).

89 To address these issues accurate estimates of the radiative heating rates of the SVC  
90 are required. Several studies have estimated SVC heating rates of a few K per day  
91 (Jensen et al., 1996a; McFarquhar et al., 2000; Comstock et al., 2002). In general, these  
92 studies estimated the heating rates with a radiative transfer model using as input the  
93 microphysical data from the limited set of in situ aircraft measurements, and optical depth  
94 and cloud boundary information from lidar measurements. Until now there has not been  
95 a direct measurement of the heating rates of subvisible cirrus to evaluate these estimates.

96 Here we present the first direct measurements of the infrared and solar heating rates  
97 of a tropical subvisible cirrus cloud sampled off the east coast of Nicaragua on 25 July  
98 2007 by the NASA ER-2 aircraft during TC4. For almost the entire flight on this day the  
99 downlooking cloud lidar on the ER-2 detected a persistent subvisible cirrus layer near the  
100 bottom of the tropopause, with mostly clear skies underneath. Fortunately, the ER-2 had  
101 a satellite downlink capability during TC4 that provided real time views on the ground of  
102 the cloud lidar data showing the presence, altitude and thickness of the SVC below the  
103 aircraft. This enabled mission scientists to vector the ER-2 pilot to the proper altitudes  
104 and coordinates to profile through the cirrus layer. Measurements from this flight of the  
105 net broadband infrared irradiance and spectrally integrated solar irradiance above, below,  
106 and through the SVC are used to directly determine the infrared and solar heating rates of  
107 the cloud. In section 2 we describe the instruments on the ER-2 that were used in this  
108 study, specifically, the Broadband IR Radiometers (BBIR), the Solar Spectral Flux  
109 Radiometer (SSFR), and the Cloud Physics Lidar (CPL). In section 3 we present the  
110 meteorological conditions on this day and the morphological and optical properties of the  
111 SVC measured by the lidar. In section 4 we illustrate the aircraft profiling strategy used



112 to sample the SVC layer. In section 5 we present the results of our measurements of the  
113 IR and solar heating rates of the subvisible cirrus. In section 6 we compare our  
114 measurements to model generated values and in section 7 we summarize our results and  
115 make suggestions for future aircraft measurements of SVC.

116

## 117 **2. Instrument Description**

### 118 **2.1. Broadband Infrared Radiometers (BBIR)**

119 The BBIRs are Kipp & Zonen CG-4 pyrgeometers (Kipp & Zonen, 2003) that have  
120 been modified to make them better suited for use on an aircraft (Bucholtz and Jonsson,  
121 2010). They have a hemispheric field-of-view and a wavelength bandpass of 4.5-42  $\mu\text{m}$ .  
122 For TC4 identical BBIRs were mounted on the top and bottom of the ER-2 fuselage to  
123 measure the downwelling and upwelling IR irradiance, respectively.

124 The modifications made to these commercially available radiometers include a new  
125 back housing that retains the front end optics and electronics of the original instrument  
126 but allows an amplifier to be mounted directly below the sensor. The signal is then  
127 amplified from the milli-Volt range to the 0-10 Volt range and the instrument is run in  
128 current loop mode, a well established technique for minimizing the effects of noise in  
129 long signal cables. This technique is especially effective in the electronically noisy  
130 environment of a research aircraft. The new housing has the cable connector on the  
131 bottom of the instrument for easier mounting onto the aircraft. It is hermetically sealed  
132 and has a pop-up pressure relief valve that allows evacuation of air from inside the  
133 instrument to prevent damage or data loss due to condensation or freezing inside the  
134 instrument dome.

135 The Kipp & Zonen pyrgeometers have features that make them attractive for aircraft  
136 use even before modification. The off-the-shelf CG-4s have a silicon dome that acts as a  
137 solar blind filter and has an ellipse shape with a full 180° field-of-view with a good  
138 cosine response. Due to the construction methods used, any solar radiation absorbed by  
139 the window is effectively conducted away, allowing accurate measurements in full  
140 sunlight and eliminating the need for any shading disk. In addition, excellent dome to  
141 body thermal coupling eliminates the need for a dome thermistor, and the calculation of  
142 the dome to body temperature offset that is required by other pyrgeometers (Kipp &  
143 Zonen, 2003; Philipona et al., 1995).

144 The BBIRs were calibrated in-house both pre- and post-mission. The calibration  
145 entailed having the BBIRs view a blackbody source whose temperature was varied. The  
146 calibration constants were then derived from a fit of the known blackbody irradiance at  
147 each temperature versus the raw BBIR signal (in Volts). The pre- and post-mission  
148 calibrations agreed to within 5% for the downlooking radiometer and to within 2% for the  
149 uplooking radiometer, showing the stability of the BBIRs over the course of TC4.

150 As an additional test, side-by-side comparisons of the up- and down-looking BBIRs  
151 used on the ER-2 were done outside under varying sky conditions. This comparison is  
152 especially important for this study because we use the net flux, or difference between the  
153 up- and down-looking radiometer measurements, in the determination of SVC heating  
154 rates. The relative error between the two instruments is therefore more important than  
155 the absolute error of each. The side-by-side comparisons showed that the two BBIRs  
156 agreed to within +/- 1.0%. Based on these calibrations and tests the accuracy of the  
157 BBIRs is estimated to be 2-5% and the precision is estimated to be 1-3%.

158



## 159 **2.2 Solar Spectral Flux Radiometer (SSFR)**

160 The SSFR (Pilewskie et al., 2003) consists of two spectroradiometers connected via  
161 fiber optic cables to optical inlets containing a miniature integrating sphere for light  
162 collection. An optical inlet was mounted on the top (zenith viewing) and bottom (nadir  
163 viewing) of the NASA ER-2 fuselage for TC4 to measure the downwelling and upwelling  
164 spectrally resolved solar irradiance, respectively. The wavelength range of the  
165 instrument, 350 to 2150 nm, encompasses 90% of incident solar radiation. This  
166 wavelength range is covered by using two spectrometers per optical inlet: a grating  
167 spectrometer with a Silicon Charged Coupled Device (CCD) array for near-ultraviolet,  
168 visible and very near-infrared (350-1000 nm, 8 nm spectral resolution) and a  
169 spectrometer with an Indium-Gallium-Arsenide linear array detector for the shortwave  
170 infrared (900-2200 nm, 12 nm resolution) wavelength range. The SSFR records a nadir  
171 and zenith spectrum every second. For the calculations of solar heating rates discussed in  
172 this paper the SSFR data was integrated over its wavelength range to give the broadband  
173 downwelling and upwelling solar irradiance.

174 The spectrometers are calibrated in the laboratory with a National Institute of  
175 Standards and Technology (NIST)-traceable blackbody (tungsten-halogen 1000W bulb).  
176 The radiometric stability of the SSFR is carefully tracked during the course of a field  
177 experiment with a portable field calibration unit with a highly stable power source and  
178 200W lamps. The calibration held to the 1 to 2% level over the course of the TC4 field  
179 mission. The radiometric calibration was adjusted for minor fluctuations measured by  
180 the field calibration from flight to flight.



181 The data were corrected for the angular response of the light collectors and for  
182 deviations of the light collector reference plane (SSFR horizon) from horizontal due to  
183 changes in aircraft attitude (pitch, roll, and heading) which can introduce artificial offsets  
184 into the measurements of the downwelling solar irradiance. No active stabilization of the  
185 radiometers was available for this experiment. Prior to correction, the data are filtered  
186 such that measurements with only moderate deviations from horizontal alignment (less  
187 than  $3^\circ$ ) are used. The downwelling solar radiation is then corrected for any tilt in the  
188 instruments by scaling the direct component of the solar radiation by the ratio of the  
189 cosine of the true solar zenith angle (determined from ephemeris data) to the cosine of the  
190 solar zenith angle with respect to the instrument (determined from the aircraft pitch, roll,  
191 and heading), and assuming an isotropic radiance distribution for the diffuse component  
192 of the solar radiation. The direct-diffuse ratio of solar radiation is estimated using a  
193 radiative transfer code - a good approximation at the high altitudes of the ER-2 where  
194 there is very little diffuse and the direct component of solar radiation dominates the  
195 diffuse component. Schmidt et al., (2010, this issue) estimate a combined systematic  
196 error in the downwelling solar irradiance (radiometric uncertainty, angular response, and  
197 attitude correction) of 7%, and an error in the upwelling solar irradiance of 3-5% .

198

### 199 **2.3. Cloud Physics Lidar (CPL)**

200 The CPL is a multi-wavelength backscatter lidar built for use on the high altitude ER-  
201 2 aircraft and was first deployed in 2000 (McGill et al., 2002; 2003). It was mounted in a  
202 wing pod on the ER-2 for TC4 and looked downward. The CPL utilizes a high repetition  
203 rate, low pulse energy transmitter and photon-counting detectors. It is designed

204 specifically for three-wavelength operation (355, 532, and 1064 nm, with depolarization  
205 at 1064 nm) and maximum receiver efficiency. An off-axis parabola is used for the  
206 telescope, allowing 100% of the laser energy to reach the atmosphere. The CPL is  
207 designed with a nominal 100 microradian field of view to minimize the effects of  
208 multiple scattering. CPL data products are typically provided at 30 m vertical resolution  
209 and 1 second horizontal resolution (~200 m at the nominal ER-2 speed of 200 m/s).  
210 Complete instrument details can be found in McGill et al. (2002).

211 The CPL fundamentally measures the total (aerosol plus Rayleigh) attenuated  
212 backscatter as a function of altitude at each wavelength. Considerable data processing is  
213 required to separate backscatter from clouds and aerosol and backscatter from Rayleigh.  
214 However, for transmissive cloud/aerosol layers, using optical depth measurements  
215 determined from attenuation of Rayleigh and aerosol scattering, and using the integrated  
216 backscatter, the extinction-to-backscatter parameter (S-ratio) can be directly derived.  
217 This permits unambiguous analysis of layer optical depth since only the lidar data is  
218 required; there is no need to use other instrumentation nor is there need for assumptions  
219 of aerosol climatology. Using the derived extinction-to-backscatter ratio, the internal  
220 cloud extinction profile can then be obtained. The error in the optical depth retrieval is  
221 estimated to be 25%, while the error in the depolarization ratio retrieval is estimated to be  
222 15%. This approach to directly solving the lidar equation without assumption is a  
223 standard analysis approach for backscatter lidar and more complete detail can be found in  
224 McGill et al. (2003).

225

226 **2.4. ER-2 Satellite Downlink (REVEAL):**



227 The TC4 mission provided an opportunity for real time flight planning and aircraft  
228 coordination. The NASA-developed Research Environment for Vehicle Embedded  
229 Analysis on Linux (REVEAL) system  
230 [www.nasa.gov/centers/dryden/research/ESCD/OTH/Tools\\_Technologies/reveal.html](http://www.nasa.gov/centers/dryden/research/ESCD/OTH/Tools_Technologies/reveal.html)  
231 was installed on all three of the NASA aircraft participating in TC4 (i.e. the ER-2, WB-  
232 57, and DC-8 aircraft). The REVEAL system permits real time reporting of the aircraft  
233 location and, more importantly, provides a means for real time downlinking of data from  
234 the aircraft instruments. The CPL onboard the ER-2 aircraft was one of the first  
235 instruments to utilize this capability of REVEAL. Although bandwidth limitations  
236 prohibited downlinking of all CPL data, the CPL profiles were temporally subsampled at  
237 ~10 second intervals and sent to the TC4 mission operations center. Real time  
238 interpretation of the CPL profiles permitted identification of subvisible cirrus layers and  
239 the aircraft could then be vectored to the correct latitude, longitude and altitude to sample  
240 the SVC.

241

### 242 **3. Overview of 25 July 2007 ER-2 Subvisible Cirrus Case Study**

243 Figure 1 shows the entire flight track of the ER-2 on 25 July 2007 overlaid on the  
244 Geostationary Operational Environmental Satellites (GOES) Visible image from 16:28  
245 UTC (about midway into the flight). The altitude profile of the ER-2 is shown in the  
246 inset of the figure. For TC4 the ER-2 was based out of the Juan Santamaria Airport near  
247 San Jose, Costa Rica. On this day the ER-2 was the only TC4 aircraft flying. Figure 1  
248 shows that, for the most part, the ER-2 flew over the apparent clear sky areas in the  
249 region avoiding the larger convective cells off the east coast of Costa Rica (except on

250 take-off and landing), and the smaller convective cell to the North off the east coast of  
251 Honduras.

252 To put the radiometric and lidar measurements into context Figure 2 shows altitude  
253 profiles of the temperature, wind direction, and wind speed as measured by the ER-2 on  
254 its initial climb out over the Caribbean (red lines) and by balloonsondes (Vömel et al,  
255 2007) launched from Alajuela, Costa Rica before (blue lines) and near the end (green  
256 line) of the flight (Selkirk et al. 2010). The balloonsonde near the end of the flight at  
257 17:05 UTC did not measure winds. Figure 2a shows that the bottom of the tropopause  
258 was at ~15 km with a small inversion between 15-16 km. Figures 2b and 2c show the  
259 winds were mostly out of the east and were stronger below the tropopause. The  
260 temperature and wind data measured from the ER-2 later in the flight (not shown here) at  
261 the location of the ER-2 profile through the SVC discussed in this paper (see Fig. 1) also  
262 showed the bottom of the tropopause was at ~15-16 km with winds mostly out of the  
263 east.

264 Figure 3 shows the CPL attenuated backscatter signal as measured from the ER-2 for  
265 the entire flight on this day. A variable, but persistent thin cirrus layer located between  
266 approximately 13-15 km is apparent for most of the flight even though the GOES visible  
267 satellite image (Figure 1) seems to indicate mostly clear skies along the flight track. The  
268 thin cirrus layer occurs just below the bottom of the tropopause as indicated in Figure 2a.  
269 The lidar data also shows that except for near the convective cloud regions it was mostly  
270 clear underneath this thin cirrus layer for the majority of the flight, with only scattered  
271 low clouds below 4 km. The ER-2 pilot reported that he could not see this thin cirrus



272 layer, even when he profiled through it. It only became apparent to him when he looked  
273 towards the horizon.

274 Figure 4 shows the midvisible (532 nm) optical depth and depolarization ratio (at  
275 1064 nm) derived from the lidar data for a representative section of the thin cirrus layer.  
276 The data is given for the flight segment (times: 16:20-16:39 UTC) that occurred right  
277 after the ER-2 had completed the profile down through the cirrus, climbed back up to  
278 altitude, and then reversed course, overflying the same flight track and locations of the  
279 profile. The optical depths and depolarization ratios in Figure 4 are therefore  
280 representative of the cirrus sampled during the profile. The optical depth of the cirrus  
281 layer varies between approximately 0.01 - 0.1 with a mean of 0.0342 and a standard  
282 deviation of 0.0328. These values are near or below the estimated minimum threshold  
283 for visual observation of the cloud. The measured depolarization ratio is approximately  
284 0.4, indicative of ice clouds.

285 The low optical depths of these thin ice clouds and their location near the bottom of  
286 the tropopause, combined with the fact that they do not show up in the visible satellite  
287 image and they were not seen by the ER-2 pilot, are all consistent with these clouds being  
288 subvisible cirrus.

289

#### 290 **4. ER-2 Subvisible Cirrus Sampling Strategy**

291 The ER-2 for TC4 was meant to serve as a remote sensing platform, or satellite  
292 surrogate, typically flying at a high, constant altitude of approximately 20 km. However,  
293 three factors came together in TC4 that provided an opportunity to directly measure the  
294 radiative heating rates of the subvisible cirrus by having the ER-2 deviate from its

295 nominal flight pattern and profile down through the cirrus layer. First, the high altitude  
296 of the SVC put them within reach of the ER-2. Second, as described in section 2.4, the  
297 ER-2 was equipped with a real-time downlooking cloud lidar that gave mission scientists  
298 on the ground the ability to direct the ER-2 to the proper coordinates and altitudes to  
299 sample the SVC. Third, the broadband IR and spectral solar irradiance radiometers on  
300 the ER-2 provided measurements of the net irradiances as a function of altitude from  
301 which the heating rates could be determined.

302 Figure 5 shows an idealized schematic of the flight profile flown by the ER-2 to  
303 sample the subvisible cirrus layer. On the initial northbound heading in the Caribbean  
304 (see Figure 1) the presence, altitude and thickness of the cirrus was detected in real-time  
305 by the cloud lidar (see Figure 3). At the very north end of that leg the ER-2 began to pass  
306 over a convective system off the east coast of Honduras. Therefore, the ER-2 was  
307 directed to reverse course, and once south of the convection, was given the altitudes to  
308 descend to in order to sample the previously seen SVC. As shown in Figure 5, the flight  
309 pattern consisted of a level leg above and below the cloud, and a descent and ascent  
310 through the cloud. To minimize the effects of tilt on the IR, and especially the solar,  
311 irradiance measurements (see discussion in Bucholtz et al. (2008)), the ER-2 pilot kept  
312 the attitude of the aircraft as 'flat' as possible throughout the pattern. That is, the pitch  
313 and the roll of the aircraft were kept to a minimum. For the majority of the pattern, even  
314 during the descent and climb, the pitch was kept below  $2^\circ$ , and the roll was kept below  $1^\circ$ ,  
315 except during the  $180^\circ$  turn to reverse course at the end of the descent to below the cloud.  
316 The measurements during this  $180^\circ$  turn are not used in the analysis below. The ER-2  
317 began its initial descent from 20 km at approximately 15:25 UTC and eventually returned



318 to its nominal altitude at approximately 16:30 UTC, so the complete "dip" maneuver into  
319 the SVC took about 65 minutes. The flight times of each leg are given in Figure 5.

320

## 321 **5. Measured Subvisible Cirrus Heating Rates**

322 The heating or cooling rate for a given layer in the atmosphere is defined as (Liou,  
323 1980):

$$324 \quad \left( \frac{\partial T}{\partial t} \right) = \frac{g}{c_p} \frac{\nabla F}{\Delta p} \quad (1)$$

325 where  $T$ =temperature (degrees Kelvin),  $t$ =time (day),  $g$ =gravitational acceleration  
326 ( $=980.616 \text{ cm sec}^{-2}$ ),  $c_p$ =specific heat at constant pressure ( $=1.004 \times 10^7 \text{ cm}^2 \text{ sec}^{-2} \text{ K}^{-1}$ ),  $\Delta p$   
327 is the difference in pressure between the lower and upper altitude boundaries of the given  
328 layer, and  $\nabla F$  is the difference between the net irradiances at the lower and upper  
329 boundaries of the given altitude layer. The broadband IR and spectrally integrated solar  
330 net irradiances measured from the ER-2 as it profiled through the SVC layer are used  
331 here to determine the heating rates of the cloud.

332 Figure 6 shows the net broadband solar irradiances determined from the spectral solar  
333 measurements of the SSFR instrument on the ER-2 as it profiled through the SVC layer.  
334 The net broadband solar irradiance is defined as the difference between the downwelling  
335 and upwelling solar irradiance at a given altitude. While the SSFR is a spectral  
336 instrument we are interested here in determining the complete solar heating rate of the  
337 SVC, therefore we have integrated the SSFR signal over its complete wavelength range  
338 in order to get broadband solar irradiances. The net solar irradiance measurements shown  
339 in Figure 6 have been normalized to a common solar zenith angle of  $24.162^\circ$  to account  
340 for the change in downwelling solar irradiance as the sun rose in the sky during this

341 portion of the flight. The data have also been corrected for the attitude (pitch, roll, and  
342 heading) of the aircraft as described in section 2.2. The solar measurements during the  
343 180° turn of the ER-2 on the below-cloud leg at ~15:48 UTC have been filtered out. The  
344 dip in the measurements near 15:44 and 15:53 correspond to a low level cloud of limited  
345 extent.

346 Ignoring these dips it can be seen that within the precision of the instrument there is  
347 no significant change in the net solar irradiance as the ER-2 profiles through the SVC  
348 layer. The net solar irradiance measurements for the above and below cloud legs are the  
349 same, and there is no change in the net solar as the ER-2 descends or ascends through the  
350 cloud. In effect, the SVC is not "seen" in the broadband solar irradiance data, indicating  
351 that there is no significant solar radiative energy being deposited into or out of the SVC  
352 layer. The  $\nabla F$  term in Eq. (1) for this case is therefore near zero, and the solar heating  
353 rate for this SVC layer is zero or negligible.

354 This is not the case for the IR measurements. Figure 7 shows the net broadband IR  
355 irradiances measured by the BBIR instruments on the ER-2 as it profiled through the  
356 SVC layer. The net broadband IR irradiance is defined as the difference between the  
357 upwelling and downwelling IR irradiance at a given altitude. As we did for the solar  
358 measurements, the IR measurements during the 180° turn of the ER-2 on the below-cloud  
359 leg at about 15:48 UTC have been filtered out. The large dip in the net irradiance at  
360 approximately 15:38 UTC and the smaller dip near 15:53 UTC correspond to lower level  
361 clouds of limited extent below the SVC (also see the lidar image in Figure 3 for these  
362 times).



363 Ignoring these dips in the data, it can be seen that the net IR irradiance at the level leg  
364 just above the cirrus is less than the net IR irradiance at the level leg just below the cirrus,  
365 and that the net IR irradiance increases approximately linearly with decreasing altitude  
366 through the cloud. Since the primary source for thermal IR radiation in the atmosphere is  
367 the Earth's surface (i.e. from below), the fact that the net IR irradiance above the cirrus is  
368 smaller than the net IR irradiance below the cirrus indicates that IR radiative energy is  
369 being deposited into the SVC layer. This IR energy will warm the layer.

370 Two methods were used to estimate the IR heating rate of the SVC layer. The first  
371 method determined the heating rate from the difference in the net IR irradiance at the  
372 level leg above and below the cirrus. For this case, the measured pressure and net IR  
373 irradiance for each of the legs were averaged. For the above cloud leg the mean pressure  
374 was 113.97 mb and the mean net IR irradiance and standard deviation were  $275.16 \pm$   
375  $3.33 \text{ W m}^{-2}$ . For the below cloud leg the mean pressure was 137.2 mb and the mean net  
376 IR irradiance and standard deviation were  $282.03 \pm 2.33 \text{ W m}^{-2}$ . The standard  
377 deviations of the net IR irradiances incorporate both the limits in the precision of the IR  
378 radiometers and the natural variability in the IR signal from the atmosphere. These values  
379 were put into Eq. (1) and using standard propagation of error analysis (Bevington, 1969)  
380 the IR heating rate was found to be:

381 
$$\text{IR Heating Rate (from level legs)} = 2.50 \pm 1.48 \text{ K day}^{-1}$$

382 The second method for estimating the IR heating rate used the net irradiance data  
383 during the descent and ascent legs of the profile. At first glance, this would appear to be  
384 a straightforward method. Simply use Eq. (1) to calculate the heating rate profile by  
385 numerically differentiating the measured net IR irradiances with respect to pressure (i.e.

409 **6. Comparison to Calculated Values**

410 The heating rates measured in this paper are consistent with previous model generated  
411 values for subvisible cirrus of comparable optical depths. For example, Jensen et al.  
412 (1996a) used a detailed cirrus cloud model and the in situ microphysical aircraft  
413 measurements from Heymsfield (1986) to estimate heating rates of 1-3 K per day for  
414 SVC with optical depths in the range of 0.01 to 0.03. McFarquhar et al. (2000) also used  
415 the Heymsfield (1986) data, plus the in situ microphysical aircraft measurements of  
416 Booker and Stickel (1982) and estimates of the SVC optical depth from the lidar on the  
417 NASA ER-2 aircraft during the CEPEX field study in 1993 as input into the Fu and Liou  
418 (1993)  $\delta$ -four-stream radiative transfer code. Estimated heating rates of 1-2 K per day for  
419 SVC with optical depths of approximately 0.01 were determined. Comstock et al. (2002)  
420 used estimates of cloud optical depth and cloud base and top heights from surface lidar  
421 measurements on Nauru Island as input into the Fu and Liou (1993) code and estimated  
422 heating rates of approximately 3 K per day for a single SVC layer with an optical depth  
423 of 0.022.

424 As a further test of the heating rates determined in this paper we computed IR and  
425 solar radiative heating rates for clear skies and for two SVC cloudy-sky cases using the  
426 Rapid Radiative Transfer Model (RRTM; Mlawer and Clough, 1997; Mlawer et al.,  
427 1997). RRTM uses a correlated-k method for gaseous absorption, the Clough Kneizys  
428 Davies (CKD) 2.4 water vapor continuum model (Clough et al., 1989), and cloud ice  
429 parameterizations based on an effective size and water content (Fu et al., 1998; Fu, 1996).  
430 The key model input parameters relevant to this study are the vertical profiles of  
431 atmospheric temperature, ozone, water vapor, and cloud microphysical properties



432 including the ice water path and a generalized effective diameter for ice ( $D_{ge}$ , e.g., eqs.  
433 3.11-3.12, Fu, 1996).

434 The vertical profiles of ozone, water vapor, and temperature are provided by the  
435 Cryogenic Frostpoint Hygrometer (CFH; Vömel et al., 2007) and ECC ozonesonde  
436 launched from the Juan Santamaria Airport in Alajuela, Costa Rica at 17 Z on 25 July  
437 2007 (Selkirk et al., 2010). The water vapor measurements extend up to about 60 mb,  
438 whereas the ozone and temperature measurements go to 10 mb. Above these levels, data  
439 from the nearest overpass of the Microwave Limb Sounder (MLS) are used. The solar  
440 zenith angle was set to  $28^\circ$ . For these RRTM model runs the cloud optical depth,  $\tau$ ,  
441 was set to zero for the clear sky case, and to 0.02 and 0.05 for the cloud cases to span the  
442 0.0342 mean optical depth of the SVC sampled in this study. The cloud was distributed  
443 over a layer 0.5 km thick for both cloud cases. Since we did not have microphysical  
444 measurements of the SVC on 25 July 2007 the effective radius,  $r_e$ , was set to  $14 \mu\text{m}$  ( $D_{ge}$   
445 =  $21 \mu\text{m}$ ) in the calculations, corresponding to the value found by in situ measurements  
446 of an SVC sampled by the WB-57 aircraft on 6 August 2007 during TC4 (Davis et al,  
447 2010, this issue).

448 Figure 9 shows the solar and IR heating rates determined for these three cases. The  
449 calculated solar heating rates (Figure 9a) for the 0.02 and 0.05 optical depth cloud cases  
450 are  $0.23 \text{ K day}^{-1}$  and  $0.37 \text{ K day}^{-1}$ , respectively, showing the minimal effect of the SVC  
451 on the solar radiation. On the other hand, the calculated IR heating rates (Figure 9b) for  
452 the 0.02 and 0.05 optical depth cloud cases are  $0.95 \text{ K day}^{-1}$  and  $2.6 \text{ K day}^{-1}$ , respectively.  
453 While still not large, this heating is significant compared to the clear sky case that has a  
454 slight IR cooling rate of  $-0.21 \text{ K day}^{-1}$ . These calculated heating rates are not expected to

455 be exactly the same as our measured values because of our lack of in situ microphysical  
456 measurements of the SVC on the 25 July, however, these calculated values are  
457 comparable to the negligible solar heating rate and the 2.5-3.24 K day<sup>-1</sup> IR heating rates  
458 determined in this paper.

459

## 460 **7. Summary**

461 In this paper we determined the infrared and solar heating rates of a tropical  
462 subvisible cirrus cloud through direct measurements of the net IR and solar irradiances  
463 above, below, and through the cloud. The measurements were made from the NASA ER-  
464 2 aircraft as it performed a rare descent profile down through an SVC layer off the east  
465 coast of Nicaragua on 25 July 2007 during the TC4 field study. The ER-2 lidar  
466 measurements showed that the variable SVC layer was located near the bottom of the  
467 tropopause at approximately 13-15 km with mostly clear skies underneath. Its midvisible  
468 optical depth varied from 0.01-0.1 with a mean of 0.0342 and a standard deviation of  
469 0.0328. Its depolarization ratio was approximately 0.4, indicative of ice clouds. The  
470 solar heating rate was found to be negligible, however, the infrared heating rate of the  
471 SVC was determined to be approximately 2.50-3.24 K day<sup>-1</sup>. These values were found to  
472 be consistent with previous indirect observations of other SVC and with model-generated  
473 heating rates of SVC with similar optical depths.

474 This direct measurement study therefore supports the current estimates that the  
475 typical heating rate of the SVC is a few K per day with most of the heating occurring in  
476 the IR. As discussed in Gage et al. (1991) heating of this magnitude can modify the  
477 dynamics of the upper troposphere and lower stratosphere by increasing upward vertical



478 motions, consequently affecting stratosphere-troposphere exchange (Corti et al., 2006),  
479 and possibly contributing to the dehydration of the lower stratosphere (Jensen et al.,  
480 1996b), or leading to an increase in water vapor in the lower stratosphere as suggested by  
481 the model simulations of Rosenfield et al. (1998). This heating is also sufficient to either  
482 warm the cloud, causing it to dissipate, or drive upward motion that lifts the cloud and  
483 causes it to persist for days (Jensen et al., 1996a). It has also been suggested by two  
484 recent studies (Durrán et al., 2009; Dinh et al., 2009), that IR heating of a few K per day,  
485 as measured in this paper, may thermally force a mesoscale circulation that maintains the  
486 SVC, as long as the ice crystals in the cloud have an initial mean radius that is less than 5  
487  $\mu\text{m}$ .

488 To address these uncertainties, and to truly determine the properties of subvisible  
489 cirrus and their effects on the thermodynamic structure of the upper troposphere, on  
490 stratosphere-troposphere exchange, and on climate requires more comprehensive and  
491 extensive measurements that include not only the radiative properties of the SVC but also  
492 the microphysical properties of the cloud, their spatial extent, and the thermodynamic  
493 state of the atmosphere. This study illustrates the utility and potential of the profiling  
494 sampling-strategy employed here. A high altitude aircraft that could make numerous  
495 profiles through multiple subvisible cirrus equipped with solar and IR broadband and  
496 spectral radiometers, a real-time cloud lidar, in situ cloud and aerosol probes, and state  
497 variable sensors would finally provide a much needed comprehensive dataset for  
498 characterizing both the radiative and microphysical properties of these ubiquitous tropical  
499 clouds.

500

500 **Acknowledgements**

501 We are grateful to Warren Gore and Tony Trias from NASA Ames Research Center  
502 for their engineering and technical support during TC4, especially with the integration of  
503 the BBIR instruments into the SSFR data acquisition system on the ER-2 aircraft. This  
504 work was supported by the NASA Radiation Sciences Program under grant no.  
505 NNH07AF56I (TC4).

506



506 **References**

- 507 Bucholtz, A., R. T. Bluth, B. Kelly, S. Taylor, K. Batson, A. W. Sarto, T. P. Tooman, and  
508 R. F. McCoy (2008), The Stabilized Radiometer Platform (STRAP) - An Actively  
509 Stabilized Horizontally Level Platform for Improved Aircraft Irradiance  
510 Measurements, *J. Atmos. Oceanic Technol.*, 25, 2161-2175,  
511 doi:10.1175/2008JTECHA1085.1.
- 512 Bucholtz, A., and H. Jonsson (2010), Modified Kipp & Zonen pyranometers and  
513 pyrgeometers for use on atmospheric research aircraft, *J. Atmos. Oceanic Technol.*, in  
514 preparation.
- 515 Booker, D. R., and P. G. Stickel (1982), High altitude tropical cirrus cloud observations,  
516 *Conf. on Cloud Physics Preprint*, 215-217, Amer. Meteor. Soc., Chicago, IL.
- 517 Bevington, P. R. (1969), *Data Reduction and Error Analysis for the Physical Sciences*,  
518 336 pp., McGraw-Hill Co., New York, New York.
- 519 Chartrand, R. (2005), Numerical differentiation of noisy, nonsmooth data, 9 pp., Los  
520 Alamos National Laboratory, Los Alamos, NM.
- 521 Clough, S. A., et al. (1989), Line shape and the water vapor continuum, *Atmospheric*  
522 *Research*, 23(3-4), 229-241.
- 523 Comstock, J. M., T. P. Ackerman, and G. G. Mace (2002), Ground-based lidar and radar  
524 remote sensing of tropical cirrus clouds at Nauru island: Cloud statistics and radiative  
525 impacts, *J. Geophys. Res.*, 107 (D23), 4714-4727, doi:10.1029/2002JD002203.
- 526 Corti, T., B. P. Luo, Q. Fu, H. Vomel, and T. Peter (2006), The impact of cirrus clouds on  
527 tropical troposphere-to-stratosphere transport, *Atmos. Chem. and Phys.*, 6 (9), 2539-  
528 2547.

529 Davis, S. M., D. Hlavka, E. Jensen, K. Rosenlof, S. Schmidt, S. Borrmann, W. Frey, P.  
530 Lawson, H. Voemel, and T. P. Bui (2010), In situ and lidar observations of subvisible  
531 cirrus clouds during TC4, *J. Geophys. Res.*, (submitted to this special issue).

532 Dessler, A. E., S. P. Palm, W. D. Hart, and J. D. Spinhirne (2006), Tropopause-level thin  
533 cirrus coverage revealed by ICESat/Geoscience Laser Altimeter System, *J. Geophys.*  
534 *Res.*, *111*(D08), 203, doi:10.1029/2005JD006 586.

535 Dinh, T. P., D. R. Durran, and T. P. Ackerman (2009), The maintenance of tropical-  
536 tropopause-layer cirrus, *J. Geophys. Res.*, submitted.

537 Durran, D. R., T. Dinh, M. Ammerman, and T. Ackerman (2009), The mesoscale  
538 dynamics of thin tropical tropopause cirrus, *J. Atmos. Sci.*, in press.

539 Fu, Q., and K. N. Liou (1993), Parameterization of the radiative properties of cirrus  
540 clouds, *J. Atmos. Sci.*, *50*, 2008-2025.

541 Fu, Q. A. (1996), An accurate parameterization of the solar radiative properties of cirrus  
542 clouds for climate models, *J. of Climate*, *9*(9), 2058-2082.

543 Fu, Q., P. Yang, W. B. Sun (1998), An accurate parameterization of the infrared radiative  
544 properties of cirrus clouds for climate models, *J. of Climate*, *11*(9), 2223-2237.

545 Gage, K. S., J. R. McAfee, D. A. Carter, W. L. Ecklund, A. C. Riddle, G. C. Reid, and B.  
546 B. Balsley (1991), Long-Term Mean Vertical Motion over the Tropical Pacific:  
547 Wind-Profiling Doppler Radar Measurements, *Science*, *254* (5039), 1771-1773.

548 Heymsfield, A. J. (1986), Ice Particles Observed in a Cirriform Cloud at -83°C and  
549 Implications for Polar Stratospheric Clouds, *J. Atmos. Sci.*, *43*, no. 8, 851-855.



550 Immler, F., and O. Schrems (2002), LIDAR measurements of cirrus clouds in the  
551 northern and southern midlatitudes during INCA (55oN, 53oS): A comparative study,  
552 *Geophys. Res. Lett.*, 29(16), 1809-1812, doi:10.1029/2002GL015077.

553 Jensen, E. J., O. B. Toon, H. B. Selkirk, J. D. Spinhirne, and M. R. Schoeberl (1996a),  
554 On the formation and persistence of subvisible cirrus clouds near the tropical  
555 tropopause, *J. Geophys. Res.*, 101(D16), 21361-21375.

556 Jensen, E. J., O. B. Toon, L. Pfister, and H. B. Selkirk (1996b), Dehydration of the  
557 upper troposphere and lower stratosphere by subvisible cirrus clouds near the tropical  
558 tropopause, *Geophys. Res. Lett.*, 23(8), 825-828.

559 Kipp & Zonen (2003), *Instruction manual CG4 pyrgeometer*, 61 pp., Kipp & Zonen,  
560 Delft, Netherlands.

561 Lawson, R. P., B. Pilson, B. Baker, Q. Mo, E. Jensen, L. Pfister, and P. Bui (2007),  
562 Aircraft measurements of microphysical properties of subvisible cirrus in the tropical  
563 tropopause layer, *Atmos. Chem. Phys. Discuss.*, 7, 6255-6292.

564 Liou, K.-N. (1980), *An Introduction to Atmospheric Radiation*, International Geophysics  
565 Series, Vol. 26, 392 pp., Academic Press, Inc., San Diego, CA.

566 Mace, G. G., Q. Zhang, M. Vaughan, R. Marchand, G. Stephens, C. Trepte, and D.  
567 Winker (2009), A description of hydrometeor layer occurrence statistics derived from  
568 the first year of merged Cloudsat and CALIPSO data, *J. Geophys. Res.*, 114,  
569 D00A26, doi: 10.1029/2007JD009755.

570 McFarquhar, G. M., A. J. Heymsfield, J. Spinhirne, and B. Hart (2000), Thin and  
571 subvisual tropopause tropical cirrus: Observations and radiative impacts. *J. Atmos.*  
572 *Sci.*, 57, no. 12, 1841-1853.

573 McGill, M., D. Hlavka, W. Hart, V. S. Scott, J. Spinhirne, and B. Schmid (2002), Cloud  
574 Physics Lidar: instrument description and initial measurement results, *App. Opt.*, 41,  
575 no. 18, 3725-3734.

576 McGill, M.J., D.L. Hlavka, W.D. Hart, E.J. Welton, and J.R. Campbell (2003), Airborne  
577 lidar measurements of aerosol optical properties during SAFARI-2000, *J. Geophys.*  
578 *Res.*, 108, doi: 10.1029/2002JD002370.

579 Mlawer, E., S. Taubman, P. Brown, M. Iacono, and S. Clough (1997), Radiative transfer  
580 for inhomogeneous atmospheres: RRTM, a validated correlated-k model for the  
581 longwave, *J. Geophys. Res.*, 102(D14), 16663-16682.

582 Mlawer, E. J., and S. A. Clough (1997), On the extension of rapid radiative transfer  
583 model to the shortwave region, *paper presented at 6th Atmospheric Radiation*  
584 *Measurement (ARM) Science Team Meeting*, U.S. Department of Energy, CONF-  
585 9603149.

586 Peter, T., B. P. Luo, M. Wirth, C. Kiemle, H. Flentje, V. A. Yushkov, V. Khattatov, V.  
587 Rudakov, A. Thomas, S. Borrmann, G. Toci, P. Mazzinghi, J. Beuermann, C.  
588 Schiller, F. Cairo, g. Di Donfrancesco, A. Adriani, C. M. Volk, J. Strom, K. Noone,  
589 V. Mitev, R. A. MacKenzie, K. S. Carslaw, t. Trautmann, V. Santacesaria, and L.  
590 Stefanutti (2003), Ultrathin tropical tropopause clouds (UTTCS): I. cloud morphology  
591 and occurrence. *Atmos. Chem. Phys.*, 3, 1083-1091.

592 Pfister, L., H. B. Selkirk, E. J. Jensen, M. R. Schoeberl, O. B. Toon, E. V. Browell, W. B.  
593 Grant, B. Gary, M. J. Mahoney, T. V. Bui, and E. Hintsä (2001), Aircraft  
594 observations of thin cirrus clouds near the tropical tropopause, *J. Geophys. Res.*,  
595 106(D9), 9765-9786.



596 Philipona, R., C. Frohlich, and C. Betz (1995), Characterization of pyrgeometers and the  
597 accuracy of atmospheric longwave radiation measurements, *Appl. Opt.*, *34*, 1598-  
598 1605.

599 Pilewskie, P., J. Pommier, R. Bergstrom, W. Gore, S. Howard, M. Rabbette, B. Schmid,  
600 P. V. Hobbs, and S. C. Tsay (2003), Solar spectral radiative forcing during the  
601 Southern African Regional Science Initiative, *J. Geophys. Res.*, *108*(D13), 8486,  
602 doi:10.1029/2002JD002411.

603 Prabhakara, C., D. P. Kratz, J. -M. Yoo, G. Dalu, and A. Vernekar (1993), Optically Thin  
604 Cirrus Clouds: Radiative Impact on the Warm Pool, *J. Quant. Spectrosc. Radiat.*  
605 *Transfer*, *49*, no. 5, 467-483.

606 Rosenfield, J. E., D. B. Considine, M. R. Schoeberl, and E. V. Browell (1998), The  
607 impact of subvisible cirrus clouds near the tropical tropopause on stratospheric water  
608 vapor, *Geophys. Res. Letts.*, *25*(11), 1883-1886.

609 Sassen, K., M. K. Griffin, and G. C. Dodd (1989), Optical Scattering and Microphysical  
610 Properties of Subvisual Cirrus Clouds, and Climatic Implications, *J. Appl. Meteor.*,  
611 *28*, 91-98.

612 Sassen, K., and B. S. Cho (1992), Subvisual-Thin Cirrus Lidar Dataset for Satellite  
613 Verification and Climatological Research, *J. Appl. Meteor.*, *31*, 1275-1285.

614 Sassen, K., and J. R. Campbell (2001), A Midlatitude Cirrus Cloud Climatology from the  
615 Facility for Atmospheric Remote Sensing. Part I: Macrophysical and Synoptic  
616 Properties, *J. Atmos. Sci.*, *58*, 481-496.

617 Schmidt, K. S., P. Pilewskie, B. Kindel, S. Platnick, M. King, G. Wind, G. T. Arnold, L.  
618 Tian, M. Wendisch (2010), Apparent and real absorption of solar spectral irradiance  
619 in heterogeneous clouds, *J. Geophys. Res.*, submitted to this special issue.

620 Selkirk, H. B., H. Vömel, J. Valverde, L. Pfister (2010), The detailed structure of the  
621 tropical upper troposphere as revealed by balloonsonde observations of water vapor,  
622 ozone, temperature and winds during the NASA TCSP and TC4 campaigns, *J.*  
623 *Geophys. Res.*, (submitted to this special issue).

624 Uthe, E. E., and P. B. Russell (1976), Lidar Observations of Tropical High-Altitude  
625 Cirrus Clouds, *IAMAP Symposium on Radiation in the Atmosphere Preprints*, 74<sup>th</sup>,  
626 Garmisch-Partenkirchen, Germany.

627 Vömel, H., D. E. David, and K. Smith (2007), Accuracy of tropospheric and stratospheric  
628 water vapor measurements by the cryogenic frost point hygrometer: Instrumental  
629 details and observations, *J. Geophys. Res.*, 112, D08305, doi:10.1029/2006JD007224.

630 Wang, P. H., P. Minnis, M. P. McCormick, G. S. Kent, and K. M. Skeens (1996), A 6-  
631 year climatology of cloud occurrence frequency from Stratospheric Aerosol and Gas  
632 Experiment II observations (1985-1990), *J. Geophys. Res.*, 101(D23), 29 407-29 429.

633 Winker, D. M. and C. R. Trepte (1998), Laminar cirrus observed near the tropical  
634 tropopause by LITE. *Geophys. Res. Letts*, 25, no. 17, 3351-3354.

635



635 **Figure Captions:**

636 **Figure 1:** The ER-2 flight track on 25 July 2007 is shown overlaid on the GOES Vis  
637 image from 16:28 UTC. The altitude profile of the ER-2 is given in the inset. The ER-2  
638 was the sole TC4 aircraft flying on this day. (Image from NASA Langley TC4 Satellite  
639 Page: <http://angler.larc.nasa.gov/tc4>).

640 **Figure 2:** Profiles of (a) temperature, (b) wind direction, and (c) wind speed as measured  
641 by the ER-2 on its initial climb out over the Caribbean (red lines) and by balloonsondes  
642 launched from Alajuela, Costa Rica before (blue lines) and near the end (green line) of  
643 the flight (Selkirk et al. 2009). All three soundings in (a) show the bottom of the  
644 tropopause at approximately 15 km with a small inversion between 15-16 km. Winds  
645 were mostly out of the East (b) and were stronger below the tropopause (c).

646 **Figure 3:** The CPL attenuated backscatter signal for the entire flight on 25 July 2007  
647 showing a persistent thin cirrus layer between approximately 13-15 km altitude. The thin  
648 cirrus layer occurs just below the bottom of the tropopause (see Fig. 2a). The ER-2  
649 headings for the different flight segments over the Caribbean are also given  
650 (N=northbound; S=southbound; W=westbound). The location of the ER-2 profile  
651 through the cirrus is indicated. The white trace shows the flight track of the ER-2 as it  
652 descends and then climbs through the SVC. The flight segment corresponding to the  
653 cloud optical depths (OD) given in Figure 4a is also indicated.

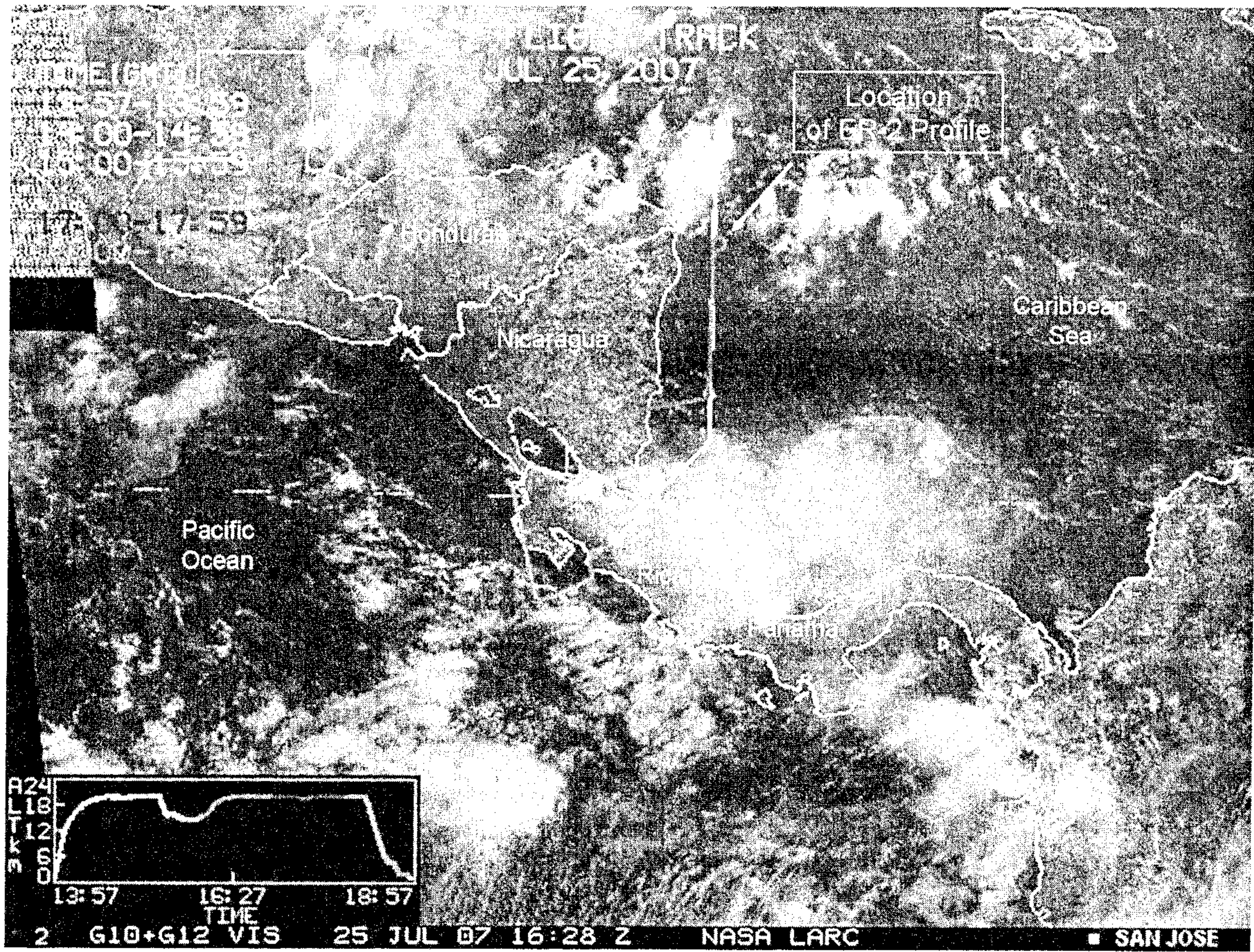
654 **Figure 4:** The (a) optical depth and (b) depolarization ratio derived from the lidar data  
655 for a representative section of the thin cirrus observed on 25 July 2007 between 16:20-  
656 16:39 UTC (see Figure 3). The optical depth of the cirrus varies between approximately  
657 0.01 to 0.1 with a mean of 0.0342 and a standard deviation of 0.0328. The estimated

680 with altitude indicates a constant IR heating rate through the layer. The slope of the  
681 linear fit (net flux per mb pressure) is used to derive the IR heating rate  
682 **Figure 9:** Calculated (a) solar and (b) IR heating rates using the RRTM radiative transfer  
683 code for clear skies and two idealized subvisible cirrus cloud cases, one with a cloud  
684 optical depth,  $\tau$ , of 0.02, and the other with a cloud optical depth of 0.05. The cloud  
685 thickness for each case was set to 0.5 km. Vertical profiles of atmospheric temperature,  
686 ozone, and water vapor from balloonsondes launched from Costa Rica on 25 July 2007,  
687 and cloud microphysical information from measurements of an SVC sampled on 6  
688 August 2009 during TC4 are used in the calculations.  
689  
690



690 Figures:

691

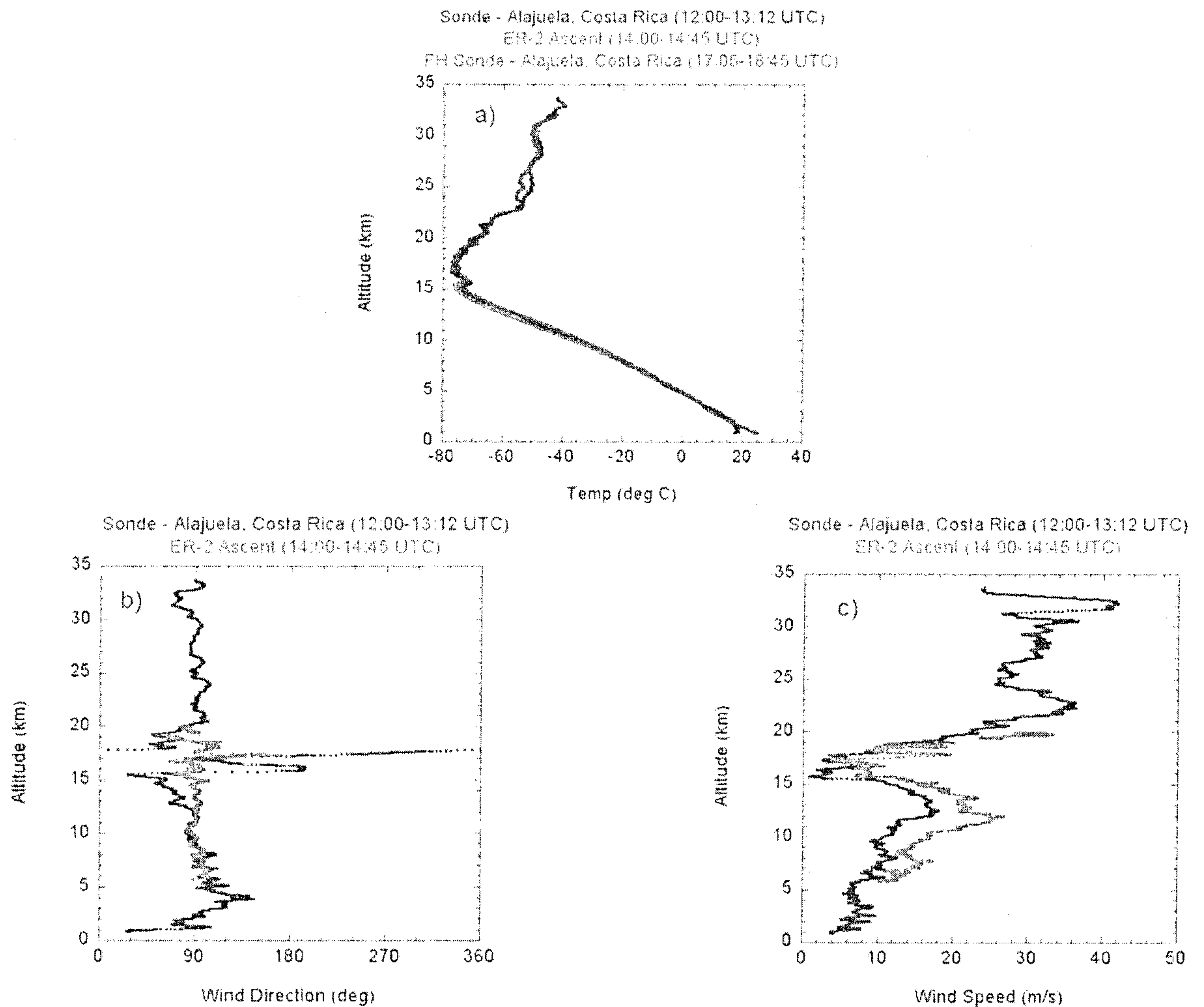


692  
693  
694  
695  
696  
697  
698  
699  
700  
701  
702

**Figure 1:** The ER-2 flight track on 25 July 2007 is shown overlaid on the GOES Vis image from 16:28 UTC. The altitude profile of the ER-2 is given in the inset. The ER-2 was the sole TC4 aircraft flying on this day. (Image from NASA Langley TC4 Satellite Page: <http://angler.larc.nasa.gov/tc4>).



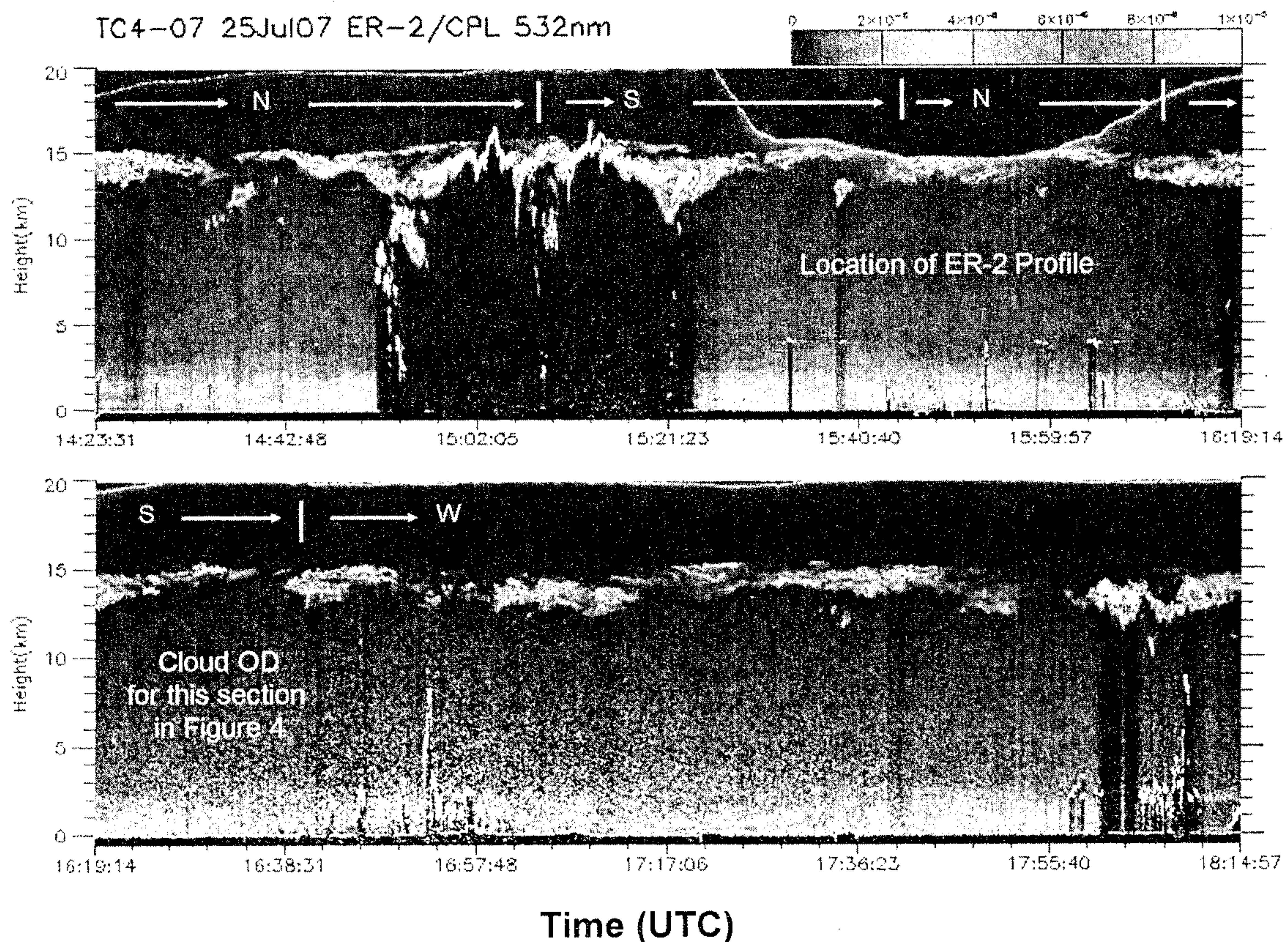
702  
703



704  
705  
706  
707  
708  
709  
710  
711  
712  
713  
714

**Figure 2:** Profiles of (a) temperature, (b) wind direction, and (c) wind speed as measured by the ER-2 on its initial climb out over the Caribbean (red lines) and by balloonsondes launched from Alajuela, Costa Rica before (blue lines) and near the end (green line) of the flight (Selkirk et al. 2009). All three soundings in (a) show the bottom of the tropopause at approximately 15 km with a small inversion between 15-16 km. Winds were mostly out of the East (b) and were stronger below the tropopause (c).



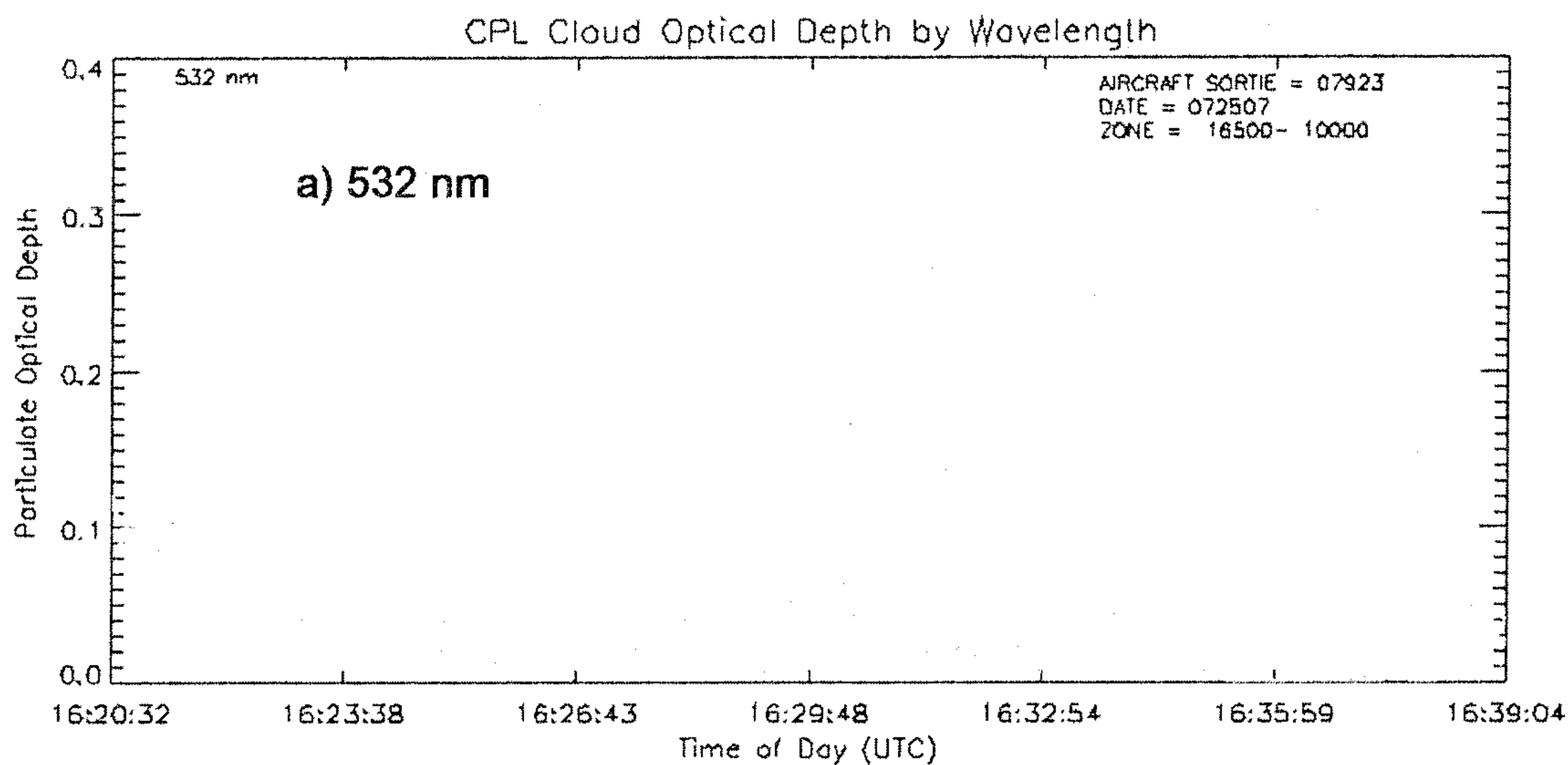


714  
715  
716  
717  
718  
719  
720  
721  
722  
723  
724  
725  
726  
727

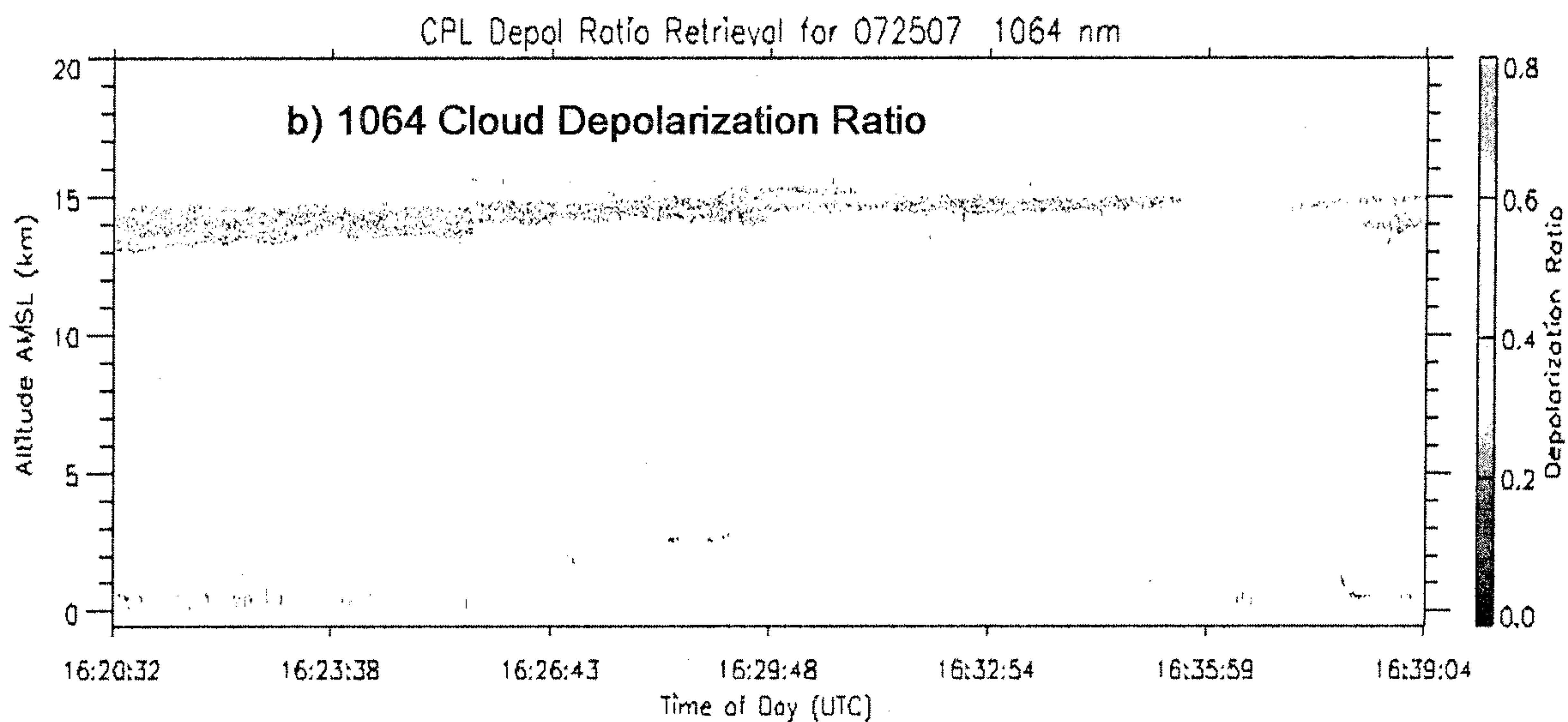
**Figure 3:** The CPL attenuated backscatter signal for the entire flight on 25 July 2007 showing a persistent thin cirrus layer between approximately 13-15 km altitude. The thin cirrus layer occurs just below the bottom of the tropopause (see Fig. 2a). The ER-2 headings for the different flight segments over the Caribbean are also given (N=northbound; S=southbound; W=westbound). The location of the ER-2 profile through the cirrus is indicated. The white trace shows the flight track of the ER-2 as it descends and then climbs through the SVC. The flight segment corresponding to the cloud optical depths (OD) given in Figure 4a is also indicated.



727



728



729

730

731

732

733

734

735

736

737

738

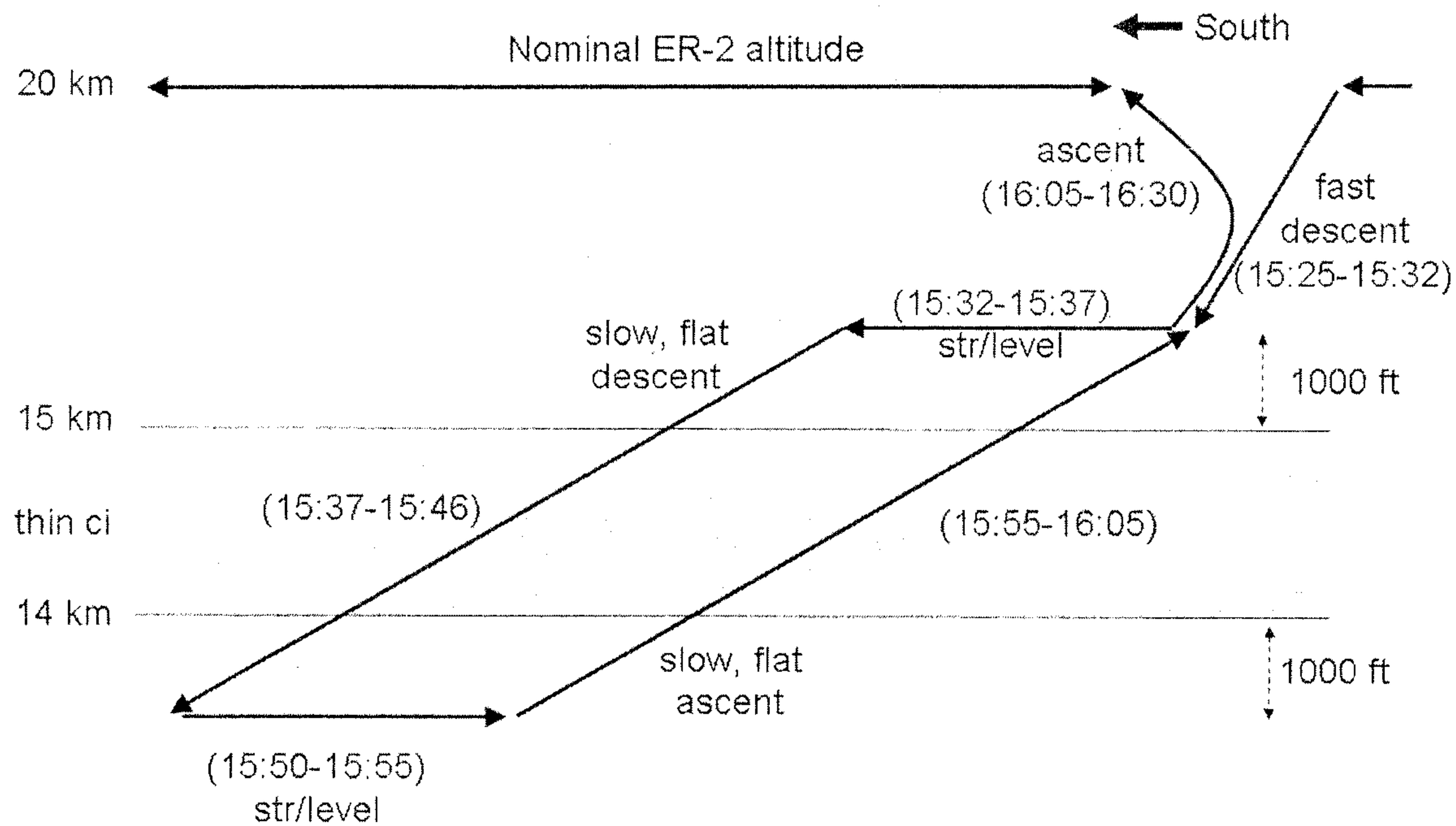
739

740

**Figure 4:** The (a) optical depth and (b) depolarization ratio derived from the lidar data for a representative section of the thin cirrus observed on 25 July 2007 between 16:20-16:39 UTC (see Figure 3). The optical depth of the cirrus varies between approximately 0.01 to 0.1 with a mean of 0.0342 and a standard deviation of 0.0328. The estimated threshold for visual observation is 0.03. The depolarization ratio (b) for these clouds is approximately 0.4 indicative of ice clouds.



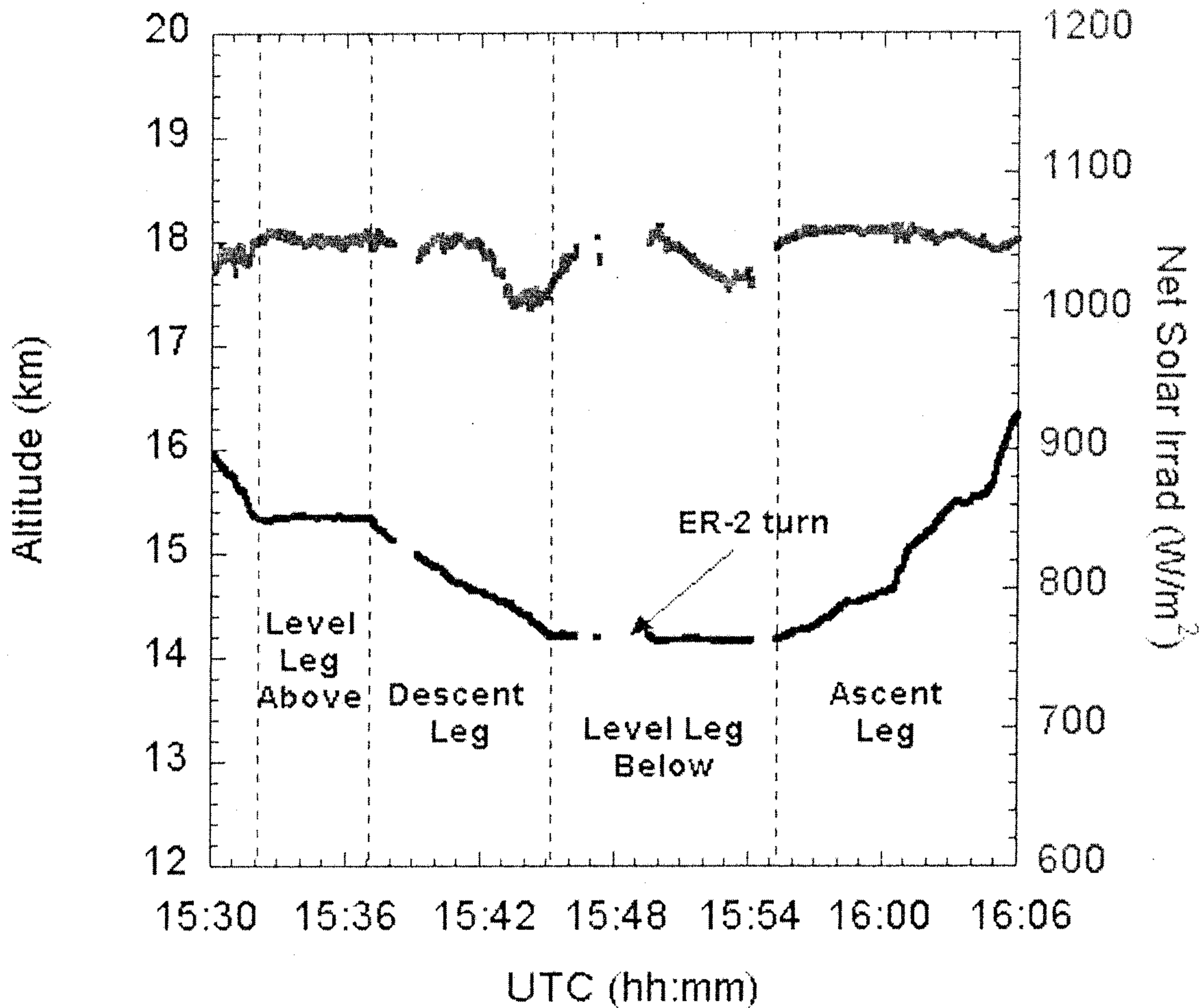
740



741  
742  
743  
744  
745  
746  
747  
748  
749  
750  
751  
752

**Figure 5:** An idealized schematic of the flight profile flown by the ER-2 to sample the subvisible cirrus layer. This flight pattern provided a level leg above and below the cloud, and a descent and ascent through the cloud to measure the IR and solar broadband net irradiances throughout the profile from which the heating rates were derived. The UTC flight times of each leg are given. The altitudes given are approximate. The actual flight pattern is shown by the white trace in Fig. 3.

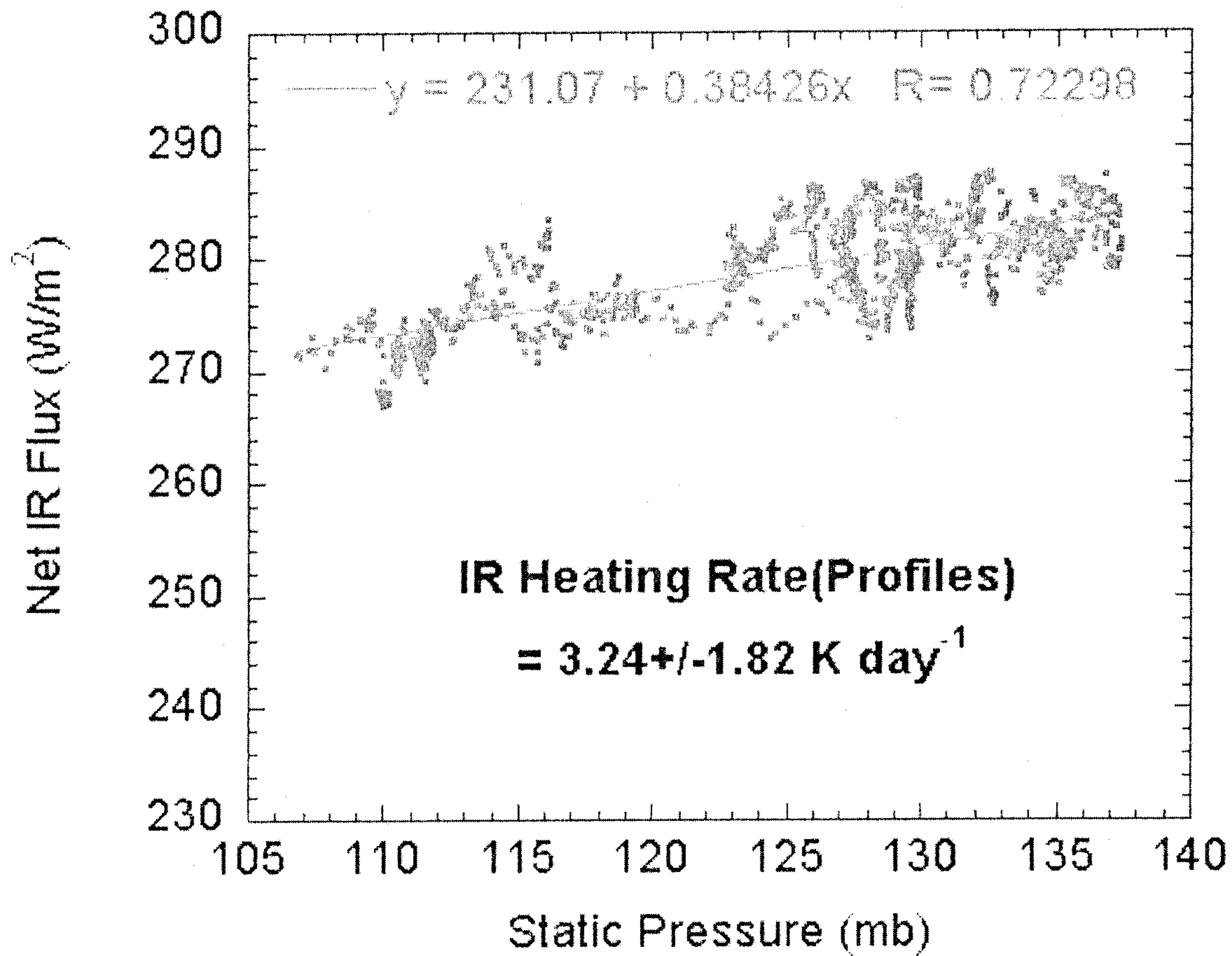
752  
753  
754  
755



756  
757  
758  
759  
760  
761  
762  
763  
764  
765  
766  
767

**Figure 6:** The net solar irradiances measured during the ER-2 profile through the subvisible cirrus and the corresponding altitudes of each leg. The net solar irradiance data for this time segment have been normalized to a solar zenith angle of  $24.162^\circ$  and corrected for the attitude (pitch, roll, and heading) of the aircraft. The measurements during the  $180^\circ$  turn of the ER-2 near 15:48 UTC have been filtered out. The dips in net irradiance at approximately 15:43 and 15:53 correspond to lower level clouds below the cirrus.

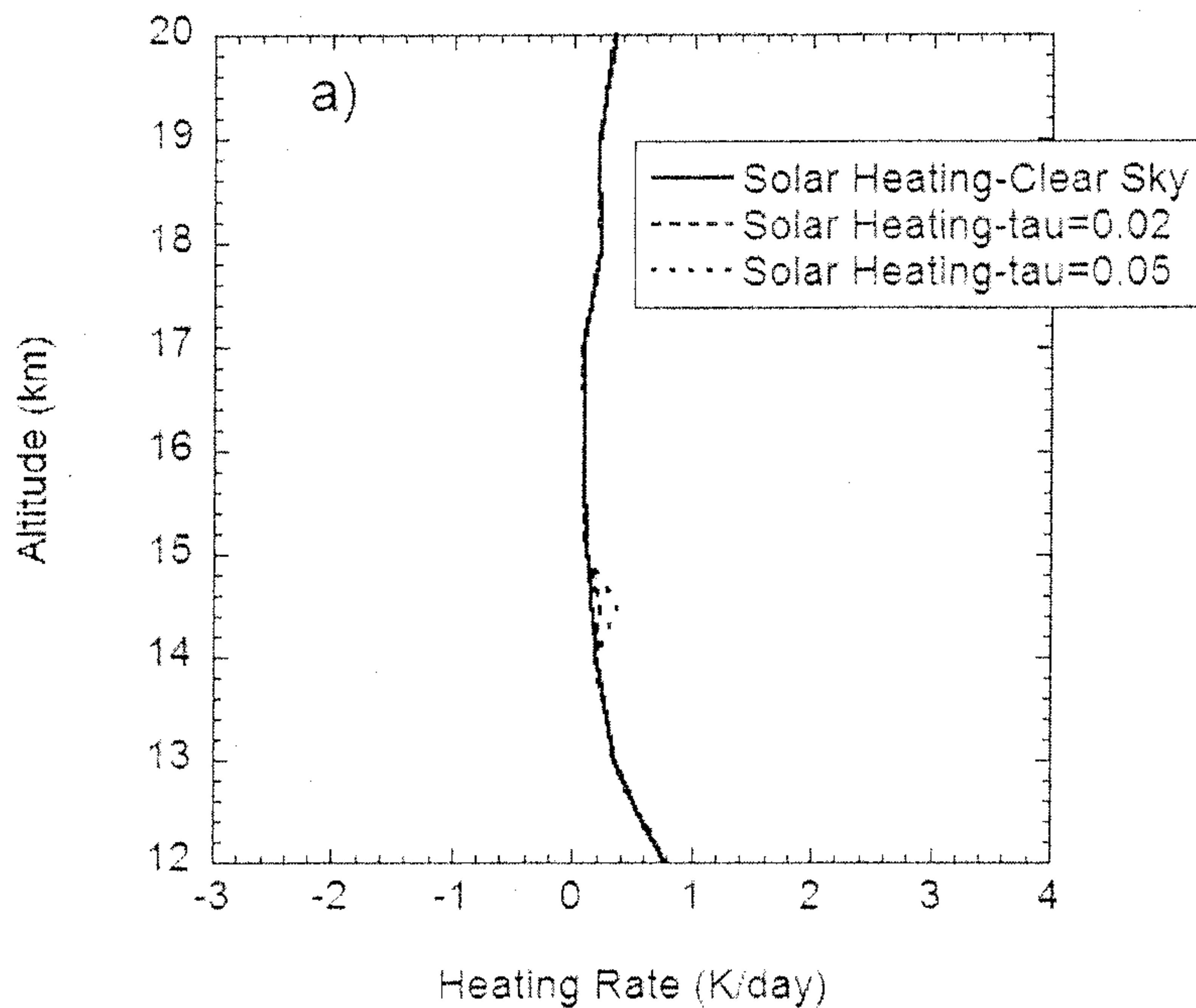




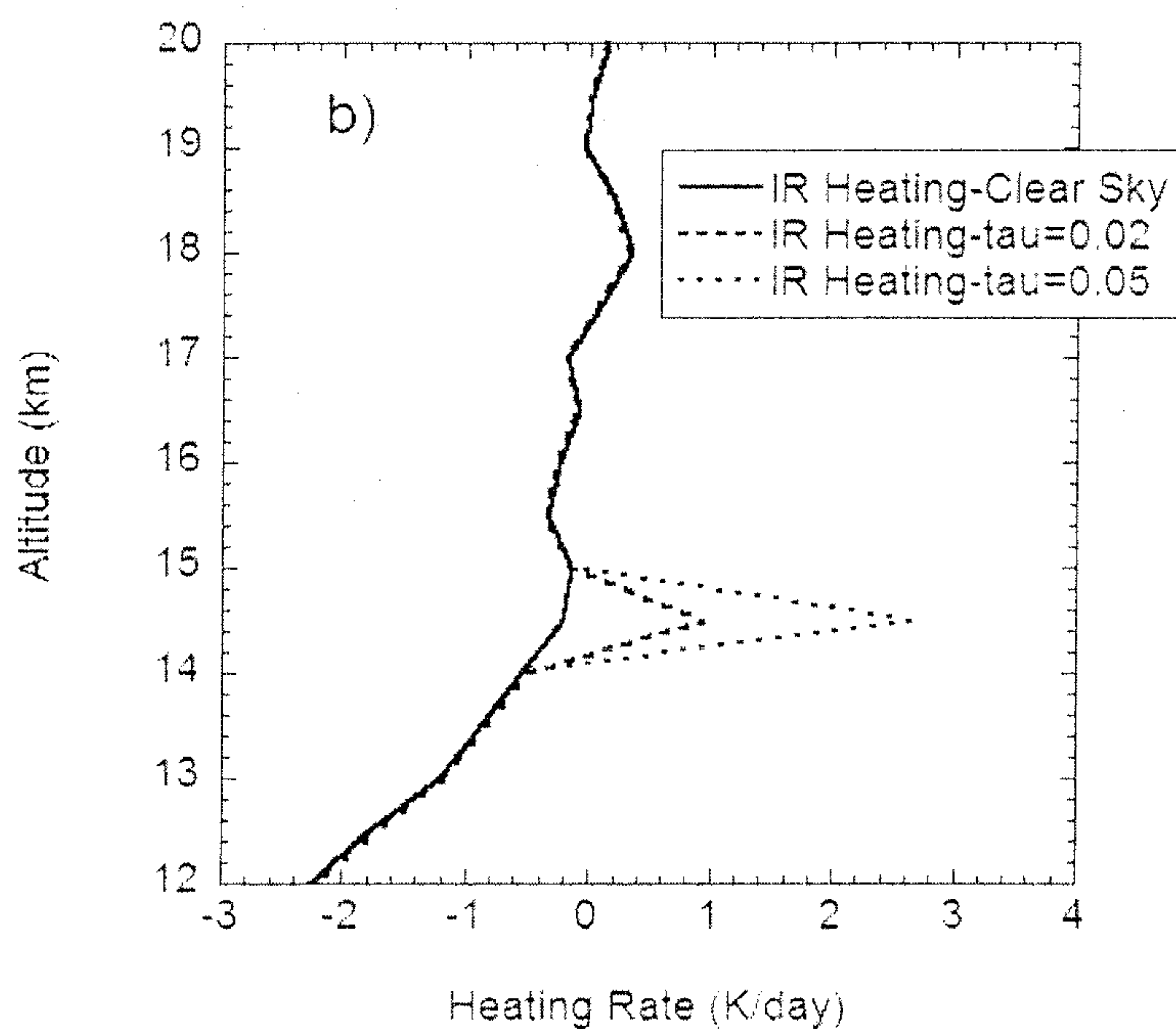
781  
 782  
 783  
 784  
 785  
 786  
 787  
 788  
 789

**Figure 8:** The net IR fluxes as a function of pressure for the descent and ascent of the ER-2 through the thin cirrus layer are combined here. The linear decrease in the net flux with altitude indicates a constant IR heating rate through the layer. The slope of the linear fit (net flux per mb pressure) is used to derive the IR heating rate

789



790  
791



792  
793  
794  
795  
796  
797  
798  
799  
800  
801

**Figure 9:** Calculated (a) solar and (b) IR heating rates using the RRTM radiative transfer code for clear skies and two idealized subvisible cirrus cloud cases, one with a cloud optical depth,  $\tau$ , of 0.02, and the other with a cloud optical depth of 0.05. The cloud thickness for each case was set to 0.5 km. Vertical profiles of atmospheric temperature, ozone, and water vapor from balloonsondes launched from Costa Rica on 25 July 2007, and cloud microphysical information from measurements of an SVC sampled on 6 August 2009 during TC4 are used in the calculations.